International Journal of Nanomedicine

Dovepress

open access to scientific and medical research

Open Access Full Text Article

ORIGINAL RESEARCH

Multifunctional Nanosnowflakes for T1-T2 Double-Contrast Enhanced MRI and PAI Guided Oxygen Self-Supplementing Effective Anti-Tumor Therapy

Yijie Lv[1], Junnan Kan[1], Mingfang Luo[2], Changfeng Yang[1], Xunrong Luo[2], Xiaoqian Lin[1], Hao Li[1], Xueming Li[1], Yuping Li[1], Caixia Yang[1], Yan Liu[1], Xianglin Li[1]

[1]School of Medical Imaging, Binzhou Medical University, Yantai, Shandong, 264003, People's Republic of China; [2]Department of Radiology, Sichuan Provincial People's Hospital, Chengdu, Sichuan, 610072, People's Republic of China

Correspondence: Yan Liu; Xianglin Li, School of Medical Imaging, Binzhou Medical University, Yantai, Shandong, 264003, People's Republic of China, Tel +86 535 6919135; +86 535 6919175, Email liuericyan@hotmail.com; xlli@bzmc.edu.cn

Introduction: Accurate tumor diagnosis is essential to achieve the ideal therapeutic effect. However, it is difficult to accurately diagnose cancer using a single imaging method because of the technical limitations. Multimodal imaging plays an increasingly important role in tumor treatment. Photodynamic therapy (PDT) has received widespread attention in tumor treatment due to its high specificity and controllable photocytotoxicity. Nevertheless, PDT is susceptible to tumor microenvironment (TME) hypoxia, which greatly reduces the therapeutic effect of tumor treatment.

Methods: In this study, a novel multifunctional nano-snowflake probe (USPIO@MnO_2@Ce6, UMC) for oxygen-enhanced photodynamic therapy was developed. We have fabricated the honeycomb-like MnO_2 to co-load chlorin e6 (Ce6, a photosensitizer) and ultrasmall superparamagnetic iron oxide (USPIO, T1-T2 double contrast agent). Under the high H_2O_2 level of tumor cells, UMC efficiently degraded and triggered the exposure of photosensitizers to the generated oxygen, accelerating the production of reactive oxygen species (ROS) during PDT. Moreover, the resulting USPIO and Mn^{2+} allow for MR T1-T2 imaging and transformable PAI for multimodal imaging-guided tumor therapy.

Results: TEM and UV-vis spectroscopy results showed that nano-snowflake probe (UMC) was successfully synthesized, and the degradation of UMC was due to the pH/ H_2O_2 responsive properties. In vitro results indicated good uptake of UMC in 4T-1 cells, with maximal accumulation at 4 h. In vitro and in vivo experimental results showed their imaging capability for both T1-T2 MR and PA imaging, providing the potential for multimodal imaging-guided tumor therapy. Compared to the free Ce6, UMC exhibited enhanced treatment efficiency due to the production of O_2 with the assistance of 660 nm laser irradiation. In vivo experiments confirmed that UMC achieved oxygenated PDT under MR/PA imaging guidance in tumor-bearing mice and significantly inhibited tumor growth in tumor-bearing mice, exhibiting good biocompatibility and minimal side effects.

Conclusion: The multimodal imaging contrast agent (UMC) not only can be used for MR and PA imaging but also has oxygen-enhanced PDT capabilities. These results suggest that UMC may have a good potential for further clinical application in the future.

Keywords: photodynamic therapy, oxygen generation, magnetic resonance imaging, photoacoustic imaging, theranostics, nanoprobe

Introduction

Cancer is still a serious threat to human health worldwide. The microenvironment during tumor growth and development is characterized by a series of abnormalities such as hypoxia, low pH, elevated oxidative stress, elevated glutathione (GSH) concentration, and enzyme overexpression. Oncology treatment may be limited by these factors, as well as providing possible avenues for cancer diagnosis and new therapeutic strategies. In recent years, different responsive nanoparticles based on the characteristics of the tumor microenvironment (TME) have been continuously developed and initially applied to the diagnosis

Received: 23 June 2022
Accepted: 17 September 2022
Published: 29 September 2022

Graphical Abstract

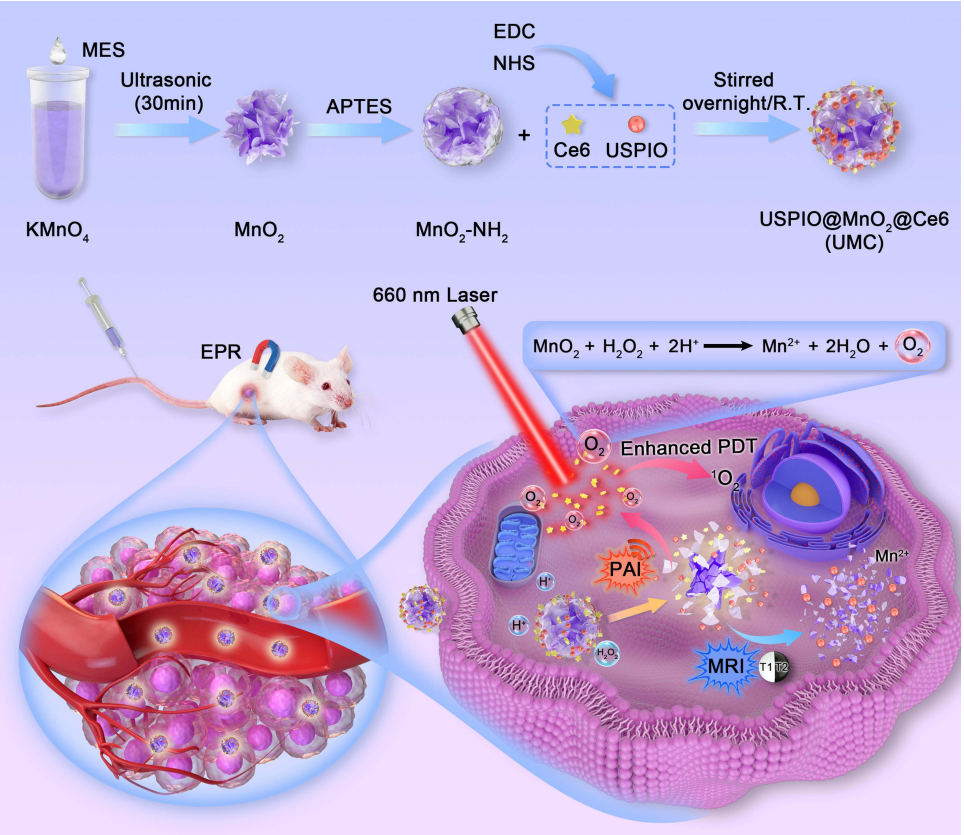

and treatment of tumors. Compared with conventional chemotherapy and radiotherapy, photodynamic therapy (PDT) is driven by photosensitizers for converting oxygen into reactive oxygen species (ROS) in the presence of an external laser to kill tumor cells. It has been considered a potential antitumor therapy due to its non-invasiveness, low systemic toxicity, high therapeutic specificity, and precise control of photocytotoxicity.[1–4] The rapid growth, volume expansion, and vascular malformation of solid tumor tissues, insufficient oxygen supply, elevated H_2O_2 levels and acidification severely limit the efficiency of oxygen-dependent PDT.[5–8] More importantly, there is an important bottleneck in the treatment of tumors, namely the change of tumor area before and after treatment, which limits the development of precision cancer treatment.

Imaging-guided PDT is a potential precision treatment option that has attracted much attention for its ability to visualize the size and location of tumors, determine treatment options, and allow clinicians to assess the effectiveness of treatment. In recent years, magnetic resonance imaging (MRI) has been widely used in clinical practice because of its high spatial and contrast resolution and nonionizing radiation characteristics. Superparamagnetic iron oxide (SPIO) nanoparticles have been widely used as T2 MRI contrast agents with high detection sensitivity.[9,10] However, ultra-small superparamagnetic iron oxide nanoparticles (USPIOs) with small crystal size (<10 nm, Fe_3O_4) are desirable to improve the biosafety. USPIOs can enter tumors site due to their enhanced permeability, and they have been reported as T1-T2 MRI double-contrast agents.[11,12] Nevertheless, this method can only distinguish micro-scale lesions with low sensitivity.[13] Photoacoustic imaging (PAI) is an emerging biomedical technology, which is promising for precise tumor localization, nanomedicine biodistribution, and deep tissue penetration. PAI can detect lesions at the molecular level and reveal rich functional information such as vascular structure and blood oxygen saturation.[14] Compared with fluorescence (FL) imaging, PAI is relatively less sensitive and difficult to perform whole-body imaging due to the limitation of acoustic transducer.[15] PA-MR dual imaging involves the fusion of an exogenous PAI contrast agent with an MRI contrast agent, allowing them to deliver complementary anatomical

and functional imaging with detectable diagnostic accuracy. MRI can observe the whole body with high precision, obtain accurate anatomy, and clarify the exact location of deep tumors. PAI shows inhomogeneous distribution of contrast agents within tumors at relatively high spatial resolution. Multimodal imaging which incorporates two or more imaging modalities into one system usually has better spatial resolution of anatomical information and highly sensitive biological information at the molecular level, yielding more accurate clinical diagnostic details than single imaging.[16] Multimodal molecular imaging probes using a variety of imaging methods precisely localize the tumors, further improve the cancer detection rates, and enhance the effectiveness of tumor treatment through synergistic effects of multiple treatments.[17] Therefore, developing a TME-responsive multimodal molecular probe is essential to provide more precise, accurate, and comprehensive imaging information.[16]

Chlorin e6 (Ce6), a prospective photosensitizer with high ROS quantum yield, near-infrared photoexcitation properties, high phototoxic potential, and low dark toxic effects, is extensively used in PDT.[18,19] However, PDT in vivo with Ce6 alone cannot efficiently induce cancer cell death due to the following reasons: 1) Low loading efficiency of photosensitizers and poor in vivo water solubility 2) In complex TME, insufficient O_2 content in cancer cells limits the therapeutic effect of PDT.[20–22] Therefore, there is an urgent need to develop a nanoprobe with high photosensitizer loading efficiency and the ability to release O_2 in response to TME. In recent years, manganese dioxide (MnO_2) nanomaterials have attracted extensive interest in developing TME-responsive and TME-modulating theranostics agents.[23] MnO_2 can react with H^+ and H_2O_2 under TME conditions [Equation (1)].[24] The generated paramagnetic Mn^{2+} significantly enhances the T1-weighted imaging for tumor-targeted detection and imaging. Insufficient oxygen concentrations in the TME can be enhanced by the decomposition of MnO_2, thus enhancing the efficacy of PDT.[25–28] Our group also reported a MnO_2-based TME-responsive nanoprobe for multimodal imaging.[29] However, most of the reported MnO_2 nanostructures were nanosheets or nanocomposites combined with other nanoparticles, which might not achieve the desired drug-loading effect.[30,31] Therefore, the development of structures with large specific surface areas, robust structures, and sufficient drug-loading capacity remains a top priority. Notably, MnO_2 has been used as a PAI, ultrasound, and photothermal imaging contrast agent.[32–34] Liu et al found that MnO_2 could also respond to TME, resulting in switchable PAI.[35] Moreover, MnO_2 nanoparticles have the advantage of favorable biocompatibility, low cost, easy preparation, and fluorescence quenching ability.[36,37] Therefore, MnO_2, as an emerging inorganic nanomaterial, has attracted extensive attention due to its advantages, such as pH/H_2O_2 responsiveness and multimodal imaging capability.

$$MnO_2 + H_2O_2 + 2H^+ \rightarrow Mn^{2+} + 2H_2O + O_2 \quad (1)$$

Based on our previous research, the constructed USPIO@MnO_2@Ce6 (UMC) nanoprobe possesses a pH/ H_2O_2-responsive capacity and follows the multimodal-imaging guided PDT (Scheme 1). UMC was well-prepared through a condensation reaction between amino (MnO_2) and carboxyl (USPIO and Ce6) groups. With the enhanced permeability and retention (EPR) effect and magnetic targeting, UMC can effectively aggregate to the tumor region and promote the decomposition of H_2O_2 to O_2, enhancing the therapeutic effect of Ce6 for PDT under laser (660 nm). We examined the main physicochemical properties of UMC and systematically investigated the efficient PDT therapy guided by ex vivo multimodal MRI/PAI. Our study highlights the importance of developing multifunctional nanoprobes for accurate multimodal imaging-guided tumor therapy.

Materials and Methods

The Synthesis and Surface Modification of Manganese Dioxide

The synthesis of MnO_2 was improved from a previous study.[38] First, 300 μL of MES buffer (pH = 6.0, 0.1 M) was added into $KMnO_4$ solution (10 mL, 10 mM) under ultrasonic conditions (40 kHz, 120 W) for 30 min. Then the solution changed from purplish red to brownish black. The product was centrifuged (12,000 rpm, 10 min) and washed twice, then resuspended in 10 mL aqueous solution. The synthesized MnO_2 product was custom synthesized with amino modification using APTES. Aqueous MnO_2 solution (1 mg/mL, 5 mL) was heated to 40°C in a water bath under N_2 protection, and then 500 μL of APTES was added and stirred overnight. The product was then washed at least 5 times with deionized water.

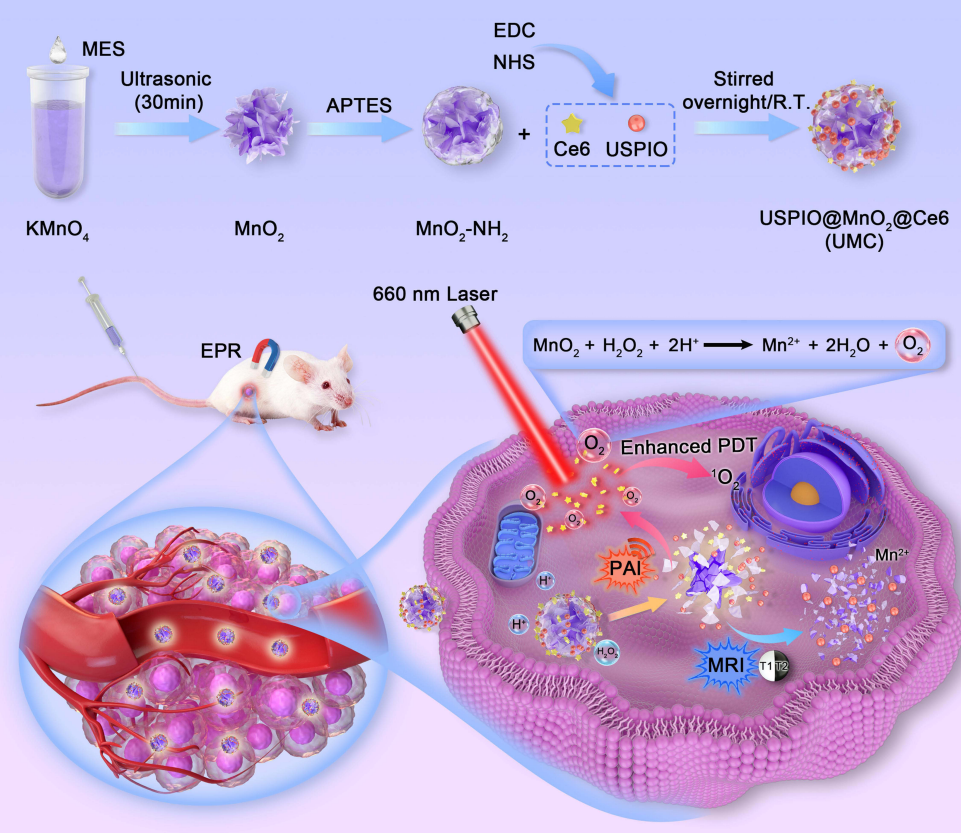

Scheme 1 Schematic illustration of the chemical synthesis process for USPIO@MnO_2@Ce6 and its mechanism of action during PDT therapy for enhanced oxygen production under the guidance of pH/H_2O_2-triggered multimodal imaging.

The Preparation of USPIO@MnO_2@Ce6

Activate USPIO-COOH (1 mg/mL, 1 mL, average diameter of approximately 5 nm, Fe_3O_4) with EDC (500 μg) and NHS (250 μg) for 25 min. The activated USPIO was further purified by washing and centrifugation. The prepared MnO_2-NH_2 (1 mL, 1 mg/mL) was added to a mixed solution containing Ce6 (80 μL, 10 mg Ce6 pre-dissolved in 1 mL DMSO solution) and USPIO (1 mL, 1 mg/mL) and stirred overnight (dark condition, for approximately 12 h) at room temperature. Next, the purified nanoparticles were obtained by washing USPIO@MnO_2@Ce6 nanoparticles (abbreviated as UMC) by centrifugation. Finally, the obtained nanoparticles were resuspended in 1 mL pure water, away from light, and stored for future use.

The Characterization of USPIO@MnO_2@Ce6

The particle size and morphology of the nanoparticles were characterized by TEM (JEM-1400, JEOL, Japan). Dynamic light scattering (DLS) measurements and zeta potential analysis of nanoparticles were performed using a Zetasizer Nano ZS (Malvern, UK). A TECAN microplate analyzer (TU 1900, Persee, China) was used to record UV-visible absorption spectra, and the fluorescence spectra was recorded with a fluorescence spectrophotometer (F-7000, Hitachi). For the synthesized nanoparticles, inductively-coupled plasma mass spectrometry (ICP-MS, Germany) was used to determine the iron and manganese concentrations. Longitudinal (T1) and transverse (T2) relaxation times and MR images were obtained using a 7.0 T MRI scanner (Biospec 70/20, Bruker, Germany). The chemical states of Fe and Mn in nanoparticles were obtained by X-ray photoelectron spectroscopy XPS (Thermo K alpha). X-ray diffraction (XRD, X`Pert PRO MPD) confirmed the phase analysis of MnO_2 and Fe_3O_4. The dissolved O_2 was detected using a portable dissolved oxygen analyzer (JPSJ-606L). The high-resolution transmission electron microscopy (HRTEM) and energy dispersive spectroscopy (EDS) analysis of UMC were performed using specific equipment (FEI, TF20, United States).

Loading and Release of Drugs

The loading of Ce6 in UMC was measured using a UV-visible absorption spectrometer (TU1900, Persee, China) at 664 nm. After centrifugation, the supernatant was removed to calculate the Ce6 content according to the standard curve. The Ce6 encapsulation rate of UMC was calculated as:

$$\text{Encapsulation efficiency} = (\text{Weight of Ce6 in UMC})/(\text{Total weightof Ce6}) \times 100\%$$

To detect the release characteristics of Ce6, UMC was resuspended in 10 mL of different solvents (pH = 7.4, 5.0, 7.4 + H_2O_2, 5.0 + H_2O_2, 100 μM) and maintained at shaker with the speed of 300 rpm. Then, 0.5 mL samples were taken at predetermined time points and centrifuged at 12,000 rpm for 20 min. Finally, the supernatant was subjected to UV-vis to calculate the release amount at different time points according to the standard curve of Ce6 at 664 nm.

Fluorescence Recovery of USPIO@MnO_2@Ce6

A fluorescence spectrophotometer (F-7000, Hitachi) was used to verify the quenching effect of MnO_2 on Ce6. The fluorescence recovery of Ce6 in different media (7.4, 5.0 + H_2O_2, 100 μM) were measured, as well as different concentrations of H_2O_2 solution and different time points.

Detection of O_2 Release and Singlet Oxygen ($^1O_2$) in vitro

A portable dissolved oxygen analyzer (JPSJ-606L) was used to monitor the oxygen production of UMC under different conditions with time to demonstrate the catalytic performance of UMC. H_2O_2 (100 μM) solutions of different pH values were added to the UMC solutions. The dissolved oxygen content was detected and recorded at predetermined time points using a portable dissolved oxygen analyzer.

A commercial assay kit, H_2DCFDA, was used to detect the production of singlet oxygen. UMC with H_2DCFDA incubation was added to the H_2O_2 (100 mM) solution. Then the solution was irradiated with 660 nm (100 mW/cm^2) laser for 5 min, and $^1O_2$ production was monitored by measuring the fluorescence intensity of H_2DCFDA recovered under 488 nm laser excitation (excitation = 488 nm, emission = 500–580 nm).

In vitro and in vivo MRI/PAI

UMC with different iron and manganese concentrations (measured by ICP) was resuspended in different pH (7.4 or 5.0) with or without H_2O_2 (100 μM), and the longitudinal (T1) and transverse (T2) relaxation times were measured by a Bruker 7.0 T MRI scanner. T1-weighted imaging parameters: repetition time (TR) = 500 ms, echo time (TE) = 18 ms, field of view (FOV) = 35 mm × 35 mm, acquisition matrix = 256 × 256, and slice thickness = 1 mm. T2-weighted imaging parameters: repetition time (TR) = 2500 ms, echo time (TE) = 30 ms, field of view (FOV) = 35 mm × 35 mm, acquisition matrix = 256 × 256, and slice thickness = 1 mm.

A multispectral photoacoustic tomography (MSOT) system (inVision-128, iThera Medical, Germany) was used to detect the PAI signals of different concentrations of UMC solutions under 650, 700, 750, 800, and 850 nm lasers. In vivo, 200 μL of UMC (USPIO: 20 mg/kg, MnO_2: 20 mg/kg) was injected through the tail vein, after which the MR and PA images were obtained at pre-specified times (0, 2, 4, 6, 8, 12, and 24 h).

Cell Culture

The 4T-1 cell line used for in vitro and in vivo experiments was acquired from American Type Culture Collection and incubated with RPMI-1640 containing 10% fetal bovine serum and 1% penicillin-streptomycin. The cells were grown in a humid environment at 5% CO_2 and 37°C.

Cellular Uptake and Cytotoxicity Assay

4T-1 cells were seeded in confocal dishes (1×10^5 cells per well) and incubated overnight. Fresh medium containing UMC (20 μg/mL) was added and incubated for different periods. Then, 4% paraformaldehyde was added to fix the cells for 20 min, and the nuclei were stained with DAPI (5 μg/mL) for 15 min. Finally, after washing the cells three times with PBS, fluorescence images of the cells were collected with a confocal laser scanning microscope (CLSM).

We used the MTT assay to monitor the cytotoxicity of UMC in vitro. 4T-1 cells were inoculated in 96-well plates at a density of 8×10^3 cells per well and incubated overnight (37°C, 5% CO_2). After removing the old medium, the cells were incubated with fresh medium containing different concentrations of free Ce6 (2 μg/mL) and UMC (equivalent to the same amount of Ce6) for 24 h. Next, the cells were washed with PBS and 10 μL of MTT (5 mg/mL) was added to each well for further incubation for 4 h. Then, 100 μL of DMSO was added to dissolve the formazan in live cells. Finally, the OD_{570} (optical density at 570 nm) was measured with a micro-reader (Spark, Tecan, Switzerland) to determine cell viability.

In vitro Therapeutic Effect and Oxygen Production of USPIO@MnO_2@Ce6

Calcein-AM/PI double staining assay to detect the therapeutic effect of UMC on 4T-1 cells. 4T-1 cells were incubated with PBS, free Ce6, and UMC (equivalent to 10 μg/mL Ce6) in the dark for 4 h. The residue in the medium was then washed off with PBS and irradiated with a 660 nm near-infrared laser (20 mW/cm^2, 3 min per well). After laser irradiation, cells were cultured in a fresh medium for an additional 4 h. Live and dead cells were stained with calcein-AM/PI staining, respectively, and observed by CLSM. For hypoxia detection, free Ce6 and UMC with different concentrations were incubated with 4T-1 cells for 4 h. Intracellular hypoxia was analyzed by CLSM using the ROS-ID Hypoxia/Oxidative Stress Detection Kit (Enzo Life Sciences) according to the manufacturer's instructions.

Animal Models

Female BALB/c mice (5–6 weeks old) were purchased from Jinan Pengyue Experimental Animal Co., Ltd., with an average weight of 18–20 grams. All animal care and experiments were performed in accordance with the Guidelines for Care and Use of Laboratory Animals of National Institutes of Health guidelines and approved by the Committee on the Ethics of Animal Experiments of Binzhou Medical University. PBS suspension (100 μL) containing 2×10^6 4T-1 cells was subcutaneously injected into the right hind limb area of BALB/c mice to establish a subcutaneous tumor model. Mice with a tumor volume of about 70 mm^3 were taken for subsequent experiments.

Antitumor Efficacy of USPIO@MnO_2@Ce6

When the tumor volume reached 70 mm^3, the tumor-bearing mice were randomly divided into 6 groups of 4 mice each: (1) PBS, (2) PBS + laser, (3) Ce6, (4) Ce6 + laser, (5) UMC, (6) UMC + laser. The injection doses were regulated at 20 mg/kg (MnO_2), 20 mg/kg (USPIO), and 16 mg/kg (Ce6). After injecting the drug (200 μL) into the tail vein for 6 h and administration of magnetic targeting, laser irradiation (660 nm, 20 mW/cm^2, 10 min) was performed, once every other day for a total of 3 treatments. The mouse's tumor volume was monitored for 14 days using the following formula:

$$\text{Tumor volume (V)} = \text{length} \times \text{width}^2/2$$

Finally, after 14 days of monitoring, the tumor-bearing mice were executed, and the main organs (heart, liver, spleen, lung, kidney) and tumors were taken and weighed. H&E staining was performed according to the standard protocols.

Statistical Analysis

All experimental results are expressed as mean ± standard deviation. The one-way analysis of variance (ANOVA) was used to evaluate the statistical significance between two or more groups, and the statistical significance was considered at a P value less than 0.05.

Results

Preparation and Characterization of USPIO@MnO_2@Ce6

We synthesized novel snowflake-like UMC (USPIO: MnO_2 weight ratio is 1:1) using a simple one-pot method. UMC was prepared through a condensation reaction between amino (MnO_2) and carboxyl (USPIO and Ce6) groups (Scheme 1). The morphology of different UMC nanoparticle fractions and the morphology of the UMC were observed by transmission electron microscope (TEM). Figure 1A shows that the average diameter of the hydrophilic spherical structure USPIO was

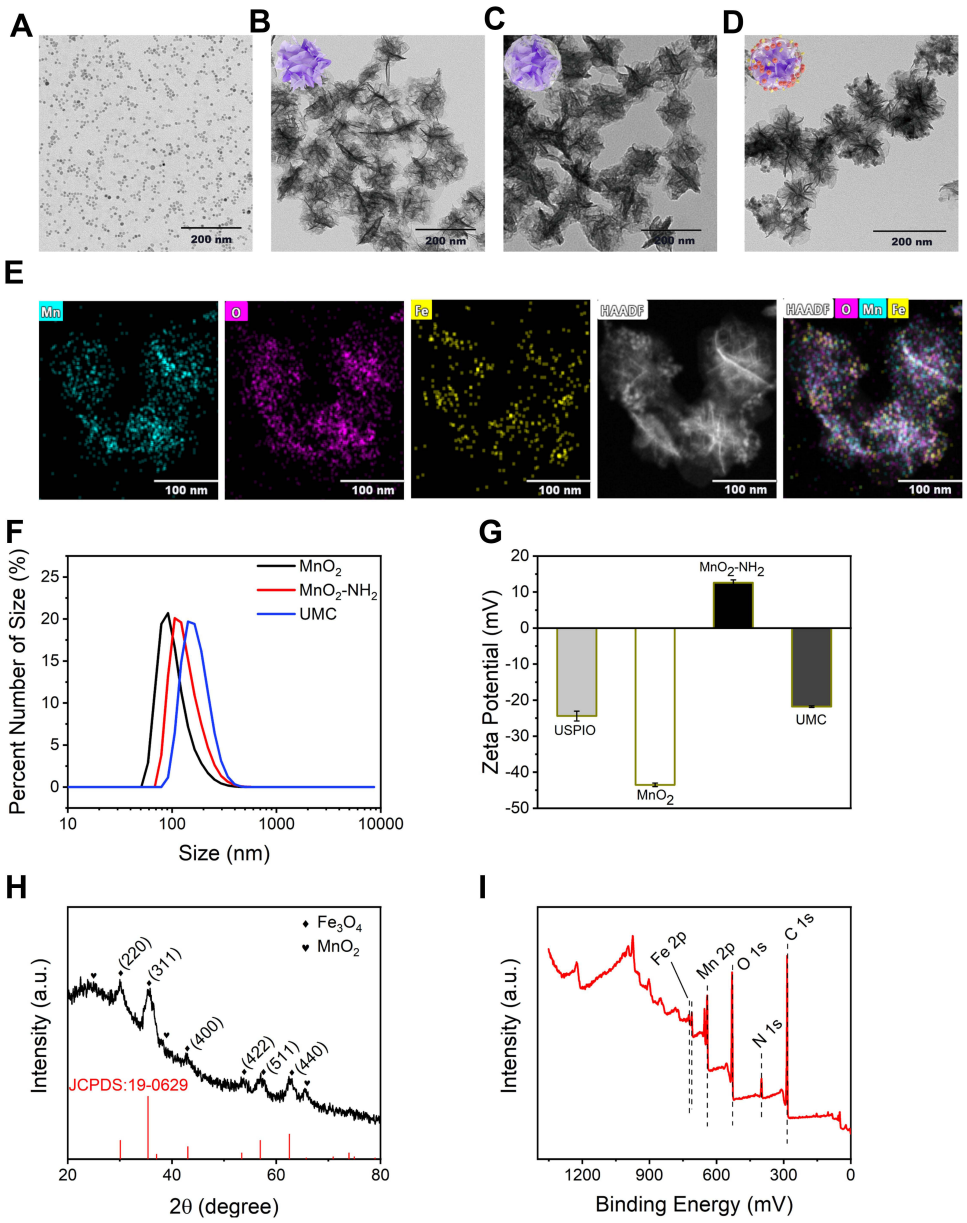

Figure 1 Characterization of the components. TEM of (**A**) USPIO, (**B**) MnO_2, (**C**) MnO_2-NH_2, and (**D**) UMC. (**E**) EDX mapping of UMC. (**F**) Dynamic light scattering (DLS) and (**G**) zeta potential of different nanoparticles. (**H**) XRD spectra and (**I**) XPS survey spectrum of UMC.

about 5 nm. The MnO_2 nanoparticles showed a uniform honeycomb design before and after the loading of amino groups (Figure 1B and C), while Figure 1D shows that each MnO_2 was connected to a multitude of USPIO particles, forming a typical "nano snowflake" structure. This result demonstrated the successful preparation of the novel snowflake nanoprobe. Elemental mapping and HRTEM further showed that USPIO anchored on the surface of MnO_2 nanoparticles (Figure 1E and S1). In addition, EDS analysis (Figure S2) showed the elemental ratios of Fe, Mn, and O were 8.9%, 48.63%, 42.47%, respectively. These results further demonstrated the presence of nanoprobes for each component of UMC and the special "Nano-Snowflakes" morphology of UMC.

The average hydrodynamic diameter and zeta potentials of MnO_2 and UMC were determined by dynamic light scattering. At pH = 7.4, the average hydrodynamic diameters of UMC and MnO_2 were 142 nm and 91 nm, respectively (Figure 1F). As shown in Figure S4, the particle sizes of UMC in Water, FBS and DMEM were 142 nm, 139.9 nm and 139.5 nm, respectively. The particle sizes of UMC did not vary significantly in different media. Figure 1G shows that the

potential of MnO_2 changed from −43.5 mV to +12.6 mV after amination, indicating successful amination modification. The zeta potential of UMC was −21.8 mV, mainly due to the negative charge of USPIO and Ce6 offsetting the positive charge of MnO_2-NH_2. The size of UMC allowed their accumulation in the tumor area through the EPR effect. As a result of hydrophilic surface interactions, the nanoparticles showed no apparent agglomeration or precipitation in a complete medium, water, and aqueous FBS solution (Figure S3). The particle size and zeta potential of UMC did not change much during the storage for 7 days. Furthermore, UMC had good stability, which contributed to its prolonged circulation time in vivo (Figure S6). The X-ray diffraction (XRD) and X-ray photoelectron spectroscopy (XPS) experiments were also performed. Figure 1H shows that the XRD patterns of UMC were consistent with MnO_2 with diffraction peaks at 2θ ~ 25.1° (002), 37.4° (111), and 65.6° (020).[39] In addition, the USPIO diffraction peaks are evident at 30.1° (220), 35.54° (311), 43.26° (400), 53.48° (422), 57.08° (511), and 62.7° (440).[40] The Mn 2p and O 1s peaks in the XPS measurement spectrum of UMC indicated the presence of +4 valence state of Mn and MnO_2 (Figure 1I). Additionally, the corresponding spectra of C, N, O, Fe, and Mn were displayed in Figure S7.

To verify the successful loading of Ce6, the UV-visible absorption spectra of Ce6, MnO_2, and UMC were detected. Figure 2A shows that MnO_2 had a broad and strong absorption at 300–600 nm with efficient fluorescence quench.[41] The characteristic absorption peak of UMC loaded with Ce6 was shifted from 664 nm to about 680 nm. The interaction between Ce6 and MnO_2 may lead to this shift. Based on the calculation of the UV-visible absorption spectroscopy standard curve (Figure S8), the loading of Ce6 could be as high as 98%. These results demonstrated the successful assembly of the three components.

Responsive Degradation of pH/H_2O_2 and Drug Release

The degradability of inorganic nanomaterials severely hinders their clinical application. Therefore, providing nanoplatforms with TME-responsiveness is crucial for precision medicine. The degradation response properties of UMC were investigated under different pH and H_2O_2. The structure of UMC nanoparticles under acidic hydrogen peroxide environment was observed by TEM. We found that the structure of the nanoflowers was degraded after the pH and H_2O_2 response (Figure 2B). The morphology of UMC changed significantly after 12 h. This result indicated that effective drug release could be achieved after UMC reaction, which was necessary for selective release in tumors. Figure 2C–E showed that when MnO_2 was combined with Ce6, the fluorescence of Ce6 was quenched. However, when UMC was co-incubated with H_2O_2 solution, the MnO_2 structure was cleaved and the fluorescence of Ce6 gradually recovered, and the fluorescence intensity of Ce6 increased with the increase of H_2O_2 solution concentration. The intensity of recovered Ce6 fluorescence increased with increasing incubation time, reaching the maximum after 15 min. Subsequently, drug release experiments were performed to study the responsive degradation characteristics of UMC and observe its release under low pH and high H_2O_2 conditions. At pH = 7.4, the cumulative release of Ce6 within 24 h was less than 10%, which was negligible. In contrast, in the acidic H_2O_2 solution (pH = 5.0), more than 20% of Ce6 was released within 24 h (Figure 2F), demonstrating the stability of the formulation.[42] The above results suggested that UMC could be degraded by H_2O_2 in a weak acid environment, leading to drug release, proving that UMC had an ultra-sensitive pH/H_2O_2 response degradation behavior.

Detection of O_2 Release and Singlet Oxygen ($^1O_2$) in vitro

Solid tumors are often in a hypoxic and weakly acidic environment due to the abnormal metabolism. Hypoxia significantly reduces the therapeutic effect of photodynamic therapy in TME, and there is an urgent need to address the problem to improve the therapeutic effect. As a non-toxic and ideal TME-responsive material, MnO_2 has been found to generate oxygen and contribute to bioimaging and therapy. MnO_2 reacts with H_2O_2 and H^+ to generate Mn^{2+} and O_2 in TME. It can be seen that compared with the H_2O_2 (0 μM) plot (Figure S5), all of MnO_2 is converted to $Mn^{2+}$and the solution color changes from dark brown to colorless, producing a large number of bubbles (O_2). However, after the reaction with pH = 5.0 + H_2O_2 buffer, the color of USPIO was not obviously changed and no bubbles were produced, indicating that USPIO could not react at pH = 5.0 + H_2O_2. The rightmost graph showed the color of UMC solution changed to yellow-green under the same condition. At this point, the MnO_2 nanoparticles in UMC were degraded, USPIO and Ce6 were released, and the solution color consisted of the yellow color of USPIO and the green color of Ce6.

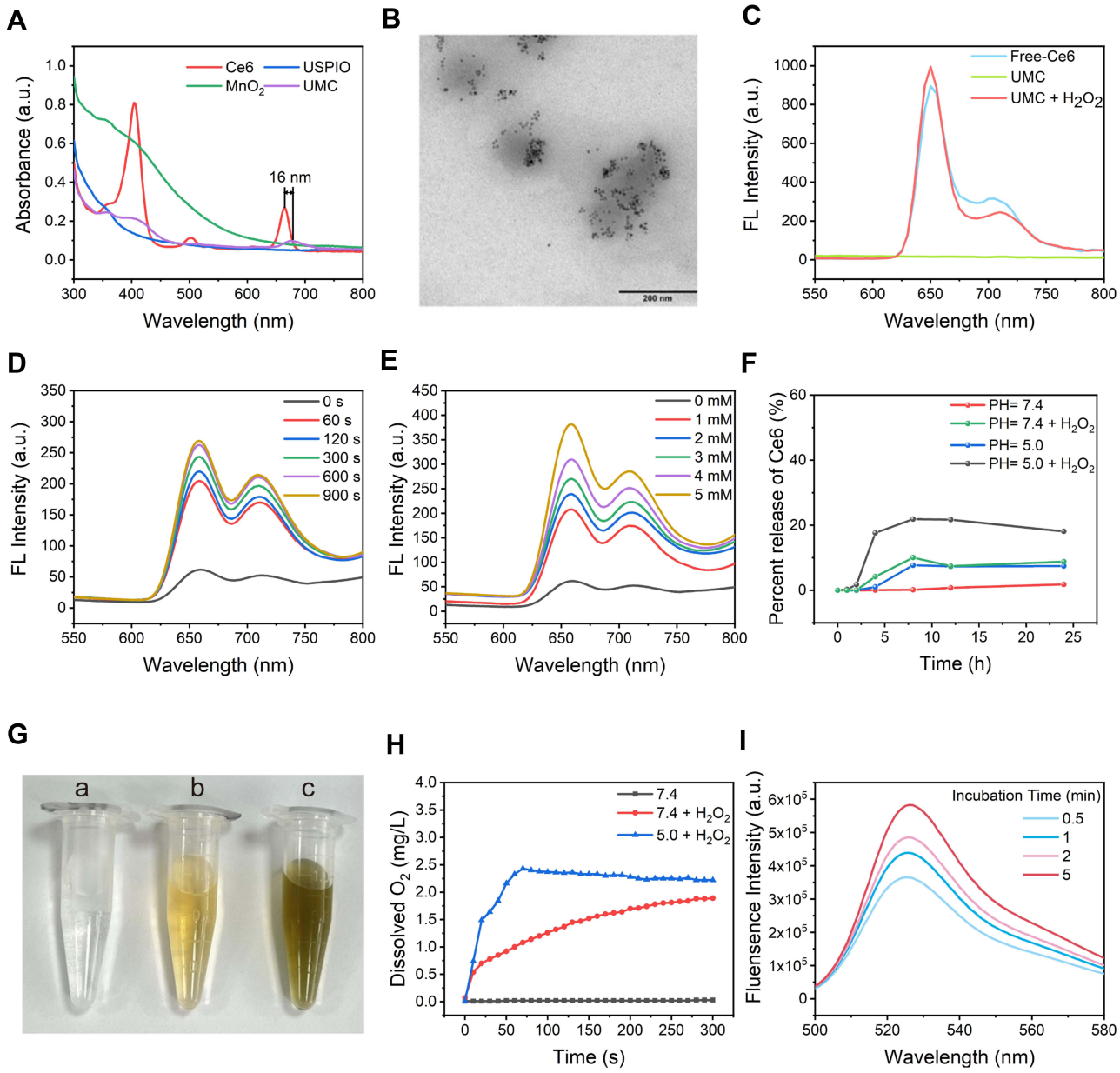

Figure 2 Extracellular pH-H_2O_2 response and detection of O_2 and $^1O_2$ production. (**A**) The UV-vis absorbance spectra of different nanoparticles. (**B**) TEM of UMC incubation with 5.0 + H_2O_2 buffer (100 μM) after 12 h. (**C**) Fluorescence spectra of the free Ce6, UMC, and UMC with H_2O_2 solution (100 μM). (**D**) The fluorescence spectra of UMC incubated with 100 μM H_2O_2 for different periods and (**E**) with different concentrations of H_2O_2 for 15 min. (**F**) The percentage of Ce6 released from UMC varied with time at different pH values (7.4 or 5.0) with or without H_2O_2 solution (100 μM). (**G**) Digital image changes of (a) MnO_2, (b) USPIO, and (c) UMC after reaction with pH = 5.0 + H_2O_2 solution (100 μM), respectively. (**H**) Oxygen generation of UMC in different solutions within 300 s. (**I**) The DCF reagent measures the formation of $^1O_2$ following laser irradiation (0.1 W/cm^2, 5 min) after co-incubation of UMC ([Ce6]: 10 μg/mL) with H_2O_2 (1 mM).

It has been shown that the concentration of H_2O_2 is about 10–100 μM in solid tumors.[43] Therefore, we measured the oxygen production after the reaction of MnO_2 with overexpressed H_2O_2 (100 μM) under different conditions (0–300 s) using a portable dissolved oxygen meter. Figure 2H shows that the oxygen production of UMC in pH = 5.0 + H_2O_2 (100 μM) solution increased rapidly within 60s and significantly higher than that of pH = 7.4 + H_2O_2 (100 μM) solution. In contrast, the oxygen production of UMC in neutral solution (pH = 7.4) was negligible, indicating that UMC might be at a relatively stable stage, causing slight damage to normal tissues.

With the increase of oxygen generated by the reaction of MnO_2 and H_2O_2, it is expected that more singlet oxygen will be generated after laser irradiation. Therefore, in the following research, we use a $^1O_2$ detection kit (H2DCFDA) to detect

the singlet oxygen produced by UMC at different time points. Figure 2I shows that we investigated the role of H_2O_2 in promoting $^1O_2$ formation. The fluorescence intensity of UMC solutions in H_2DCFDA was significantly enhanced with the increase of H_2O_2 incubation time, which was attributed to the reaction of UMC with H_2O_2 to produce more O_2, resulting in a significant increase in $^1O_2$ levels. These results confirmed the importance of UMC nanoparticles in enhancing the effect of PDT in vitro and in vivo.

TME-Responsive MRI/PAI Capacity of USPIO@MnO_2@Ce6

Numerous studies have shown that MnO_2 is an excellent TME-responsive carrier that consumes excess H_2O_2 and releases Mn^{2+} in solid tumors (which can be used as a T1 MRI contrast agent). MnO_2 has also been reported to be an excellent PAI agent at 750 nm.[35] Since MnO_2 can be degraded, the excess H_2O_2 in TME enhances the potential of UMC as a switchable MR/PA imaging agent. First, we assessed the PA imaging capabilities of UMC. Figure 3A–B showed that the PAI signal increased with the UMC concentration, and the signal intensity varied from weak to strong. In addition, the photoacoustic signal gradually weakened when UMC reacted with different concentrations of H_2O_2 solution, indicating that UMC was able to facilitate photoacoustic conversion.

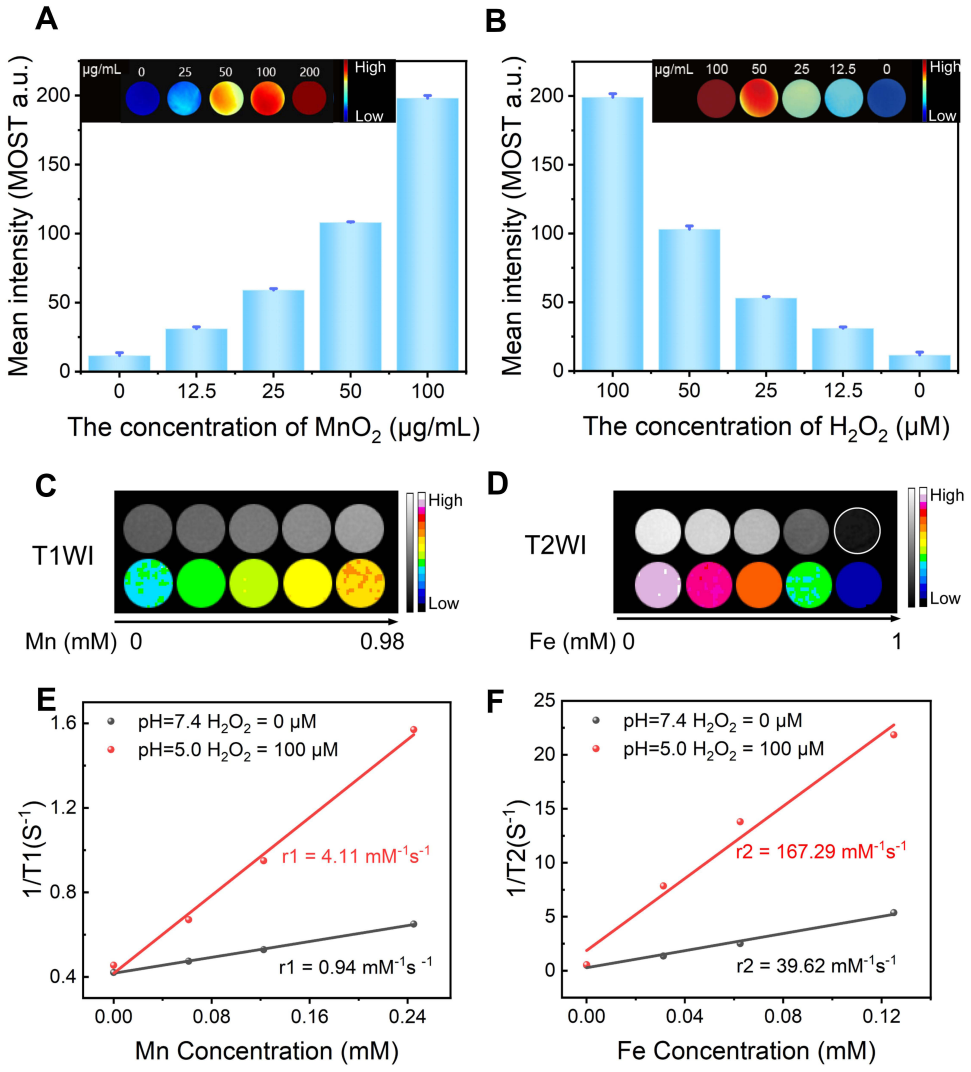

Figure 3 In vitro MR/PA imaging in response to pH-H_2O_2. (**A**) Signal changes of different concentrations of UMC solution ([MnO_2]: 0–100 μg/mL) under photoacoustic imaging. Inset: PAI images of UMC solutions with different concentrations ([MnO_2]: 0–200 μg/mL). (**B**) PAI signal changes of UMC solution ([MnO_2]: 100 μg/mL) after incubation with different concentrations of H_2O_2 solution (0–100 μM). (**C**) T1- and (**D**) T2-weighted images of UMC solutions at different pH values and concentrations of H_2O_2 solutions. (**E**) r1 and (**F**) r2 relaxation rate of UMC with different concentrations of manganese (Mn) and iron (Fe) under different conditions.

Considering that weak acids and H_2O_2 trigger UMC dissociation, which is promising for activatable MRI contrast. MRI was performed after incubation of UMC with different conditioned buffers and T1 or T2 relaxation times were measured. Figure 3C–D demonstrated that UMC had an excellent T1-T2 double contrast effect on MRI in a neutral environment. r1 relaxation rate of UMC increased from 0.94 $mM^{-1}s^{-1}$ to 4.11 $mM^{-1}s^{-1}$ for H_2O_2 dissolution conditions ranging from 0 to 100 μM (Figure 3E). In contrast, the r2 relaxation rate of UMC seemed to increase significantly from 39.62 $mM^{-1}s^{-1}$ to 167.29 $mM^{-1}s^{-1}$ (Figure 3F), indicating a good relationship between MRI signal and TME. This may be related to the release of Mn^{2+} and the aggregation state of USPIO.[44] These results suggested that UMC had excellent MR/PA imaging potential in TME.

Assessment of the Cellular Uptake and Reactive Oxygen Species (ROS) Generation

We used confocal laser microscopy to confirm that UMC (equivalent to simple Ce6: 20 μg/mL) could be efficiently taken up by 4T-1 cells. Confocal fluorescence images (Figure 4A) showed that the cell nucleus was stained blue by DAPI. Additionally, a red fluorescence signal of Ce6 could be observed in the cytoplasm, indicating that the UMC was easily absorbed by the cells and evenly distributed in the cytoplasm. The concentration of internalized Ce6 increased with increasing incubation time, and the fluorescence intensity was the strongest in the cytoplasm at 4 h (Figure 4B), indicating that the cellular uptake of UMC reached the maximum level. This time point was used in subsequent experiments.

Since UMC can release oxygen upon entry into tumor cells, they can enhance the production of singlet oxygen after laser irradiation (660 nm). Therefore, we co-incubated free Ce6 and UMC nanoparticles with cells in the laser irradiated or non-irradiated state to observe the production of singlet state oxygen in different treatment groups by CLSM. H_2DCFDA, a substance that oxidizes intracellular $^1O_2$ under laser irradiation (488 nm), can directly demonstrate the fluorescence signal generated by oxidized DCF by SLCM. Figure 5D shows no fluorescence signal in the control group (with or without laser irradiation). In contrast, a bright green fluorescent signal could be observed in the UMC group after 660 nm laser irradiation, even stronger than the free Ce6 group (same amount of Ce6). This is mainly due to the fact that MnO_2 can react with the overexpressed H_2O_2 in TME to produce O_2, which further enhances the yield of $^1O_2$.

Cell Cytotoxicity and the Photodynamic Therapy Effect in vitro

The confocal results showed that UMC and free Ce6 had an excellent cellular uptake effect, and the cytotoxicity of UMC and free Ce6 was detected by MTT method. As shown in Figure 4C, the cell viability of 4T-1 cells was inhibited by nearly 70% when the concentration was increased to 5 μg/mL after co-incubation with free Ce6 for 24 h without laser

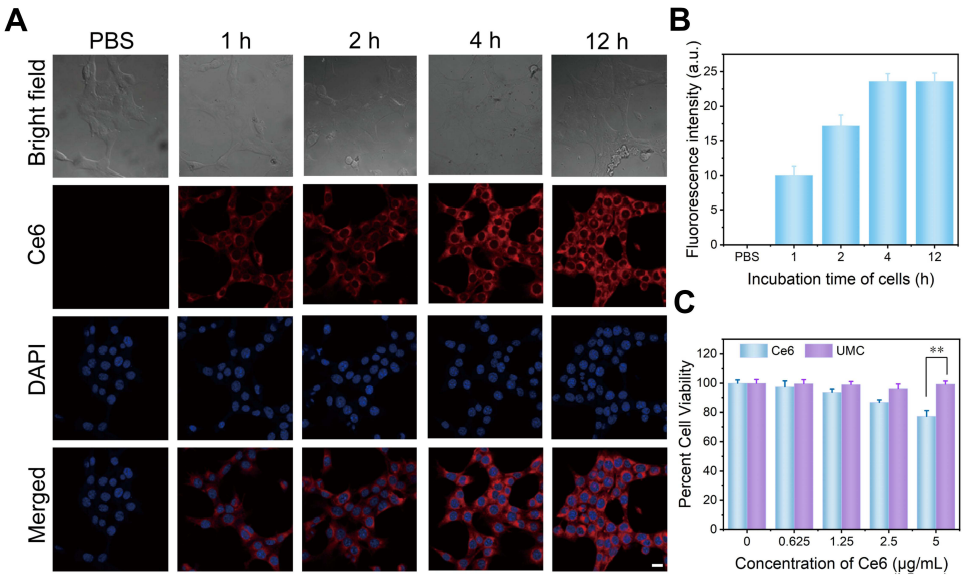

Figure 4 Cellular uptake and toxicity without laser. (**A**) Confocal images and (**B**) fluorescence intensities (scale bar: 20 μm) of UMC-treated 4T-1 cells at 1, 2, 4, and 12 h. (**C**) Cytotoxicity of 4T-1 cells treated with free Ce6 and UMC for 24 h. **Indicates $P < 0.01$ between different groups.

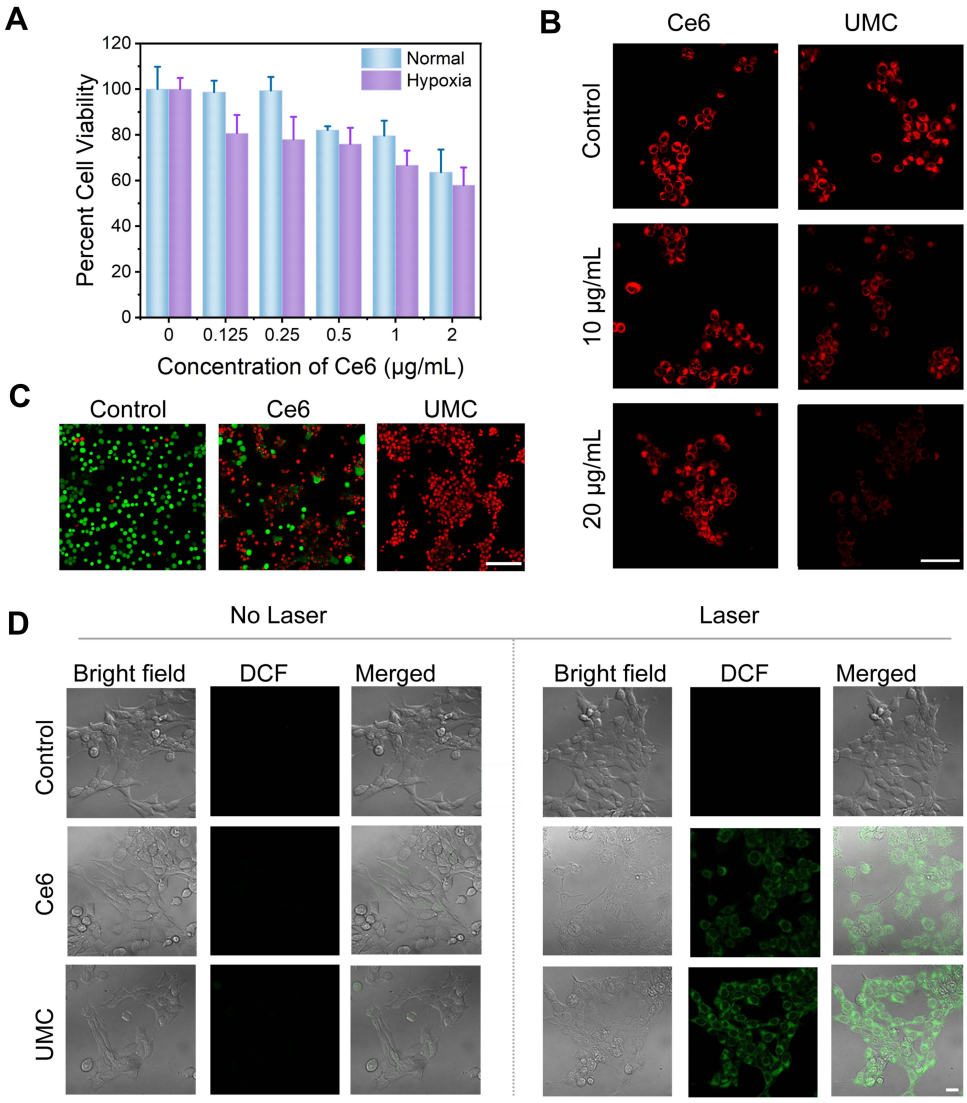

Figure 5 In vitro therapeutic effects and ROS production. (**A**) In normal and hypoxic conditions, the cell viability was influenced by UMC with laser treatment (20 mW/cm^2, 3 min). (**B**) A ROS-ID hypoxia detection probe measured the intracellular fluorescence detection of 4T-1 cells in different treatment groups. Scale bar: 50 μm. (**C**) Fluorescence images of calcein-AM/PI staining after 660 nm laser irradiation (20 mW/cm^2, 3 min) of different treatment groups ([Ce6]: 10 μg/mL) after co-incubation with 4T-1 cells. Scale bar: 100 μm. (**D**) Detection of singlet oxygen production in 4T-1 cells using DCF in different treatment groups ([Ce6]: 10 μg/mL) with or without laser irradiation (20 mW/cm^2, 3 min). Scale bar: 20 μm.

irradiation. Meanwhile, the cytotoxicity of UMC was negligible, indicating the good biocompatibility of UMC. Since cellular uptake was maximal at 4 h, we evaluated in vitro the therapeutic effect of free Ce6 and UMC solutions co-incubated with cells for 4 h under normoxic and hypoxic conditions. Photodynamic therapy was performed with a laser (660 nm, 20 mW/cm^2, 3 min), and the phototoxicity of cells was also detected by MTT method. Figure S9 showed that the therapeutic effect of different concentrations of free Ce6 was lower than normoxia under hypoxia because of oxygen limitation. This also verifies that the hypoxic state of the TME can significantly reduce the photodynamic therapeutic effect of nanoprobes. UMC had a good cell-killing effect after laser irradiation, mainly because UMC can react with the overexpressed H_2O_2 in TME to generate oxygen continuously. Due to the hypoxic characteristics of TME, Figure 5A shows that UMC still had excellent cell-killing effect under hypoxic conditions.

Cellular Therapeutic Effect and Oxygen Production in vitro

Considering the good biocompatibility, strong cellular uptake and efficient $^1O_2$ production in 4T-1 cells, we systematically evaluated the therapeutic effects of different nanoparticles in vitro to further validate the anticancer effect of

UMC. Confocal images of live and dead cells after staining (Figure 5C) showed that PBS-treated cells had almost no damaged cells, suggesting that laser basal power intensity irradiation was safe for cells. Dead cells (red staining) appeared in the free Ce6 group after laser irradiation (660 nm, 20 mW/cm^2, 3 min), suggesting that free Ce6 had a partial killing effect on 4T-1 cells. After PI (red) staining, almost all of the UMC-treated cells died, demonstrating that UMC had an outstanding laser irradiation-mediated PDT effect.

For the hypoxia assay results (Figure 5B), the fluorescence signal of UMC-treated cells was significantly reduced compared with the control group. Additionally, the hypoxia fluorescence signal decreased more obviously with the increase of UMC concentration, demonstrating its solid oxygen production capacity. It is suggested that the presence of UMC can effectively promote oxygen production and increase oxygen partial pressure, thus improving the therapeutic effect of PDT.

In vivo Imaging

After demonstrating the combined therapeutic effect of UMC in vitro, we explored its imaging effect on a tumor-bearing mouse model. After mice were injected with different treatment groups (PBS, UMC [USPIO: 10 mg/kg]) in tail vein, images of tumor areas were acquired at predefined time points (0, 2, 4, 6, 8, 12, 24 h) to monitor the accumulation of UMC. Mice with tumor volume reached 70–100 mm^3 were randomly divided into blank control and UMC groups. Figure 6B and D showed that the UMC group exhibited a significantly negative enhancement effect after 6 h post-injection, with low signal in T2-weighted images. The T1-weighted images also showed bright signals at corresponding time points. This is mainly due

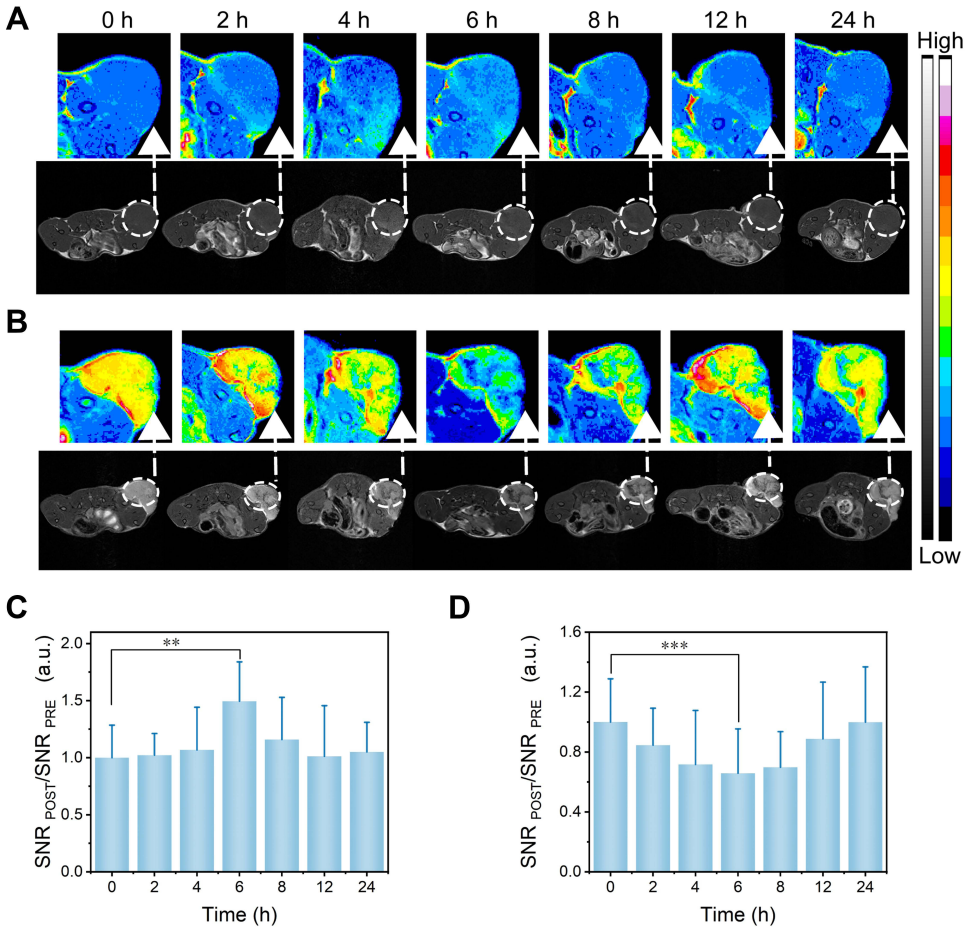

Figure 6 In vivo MR imaging. (**A**) T1- and (**B**) T2-weighted images of tumor-bearing mice at 0, 2, 4, 6, 8, 12, and 24 h after intravenous tail injection of UMC (USPIO: 20 mg/kg, MnO_2: 20 mg/kg). Quantification of the (**C**) T1 and (**D**) T2 signal changes at the corresponding time points. $^{**}P < 0.01$ and $^{***}P < 0.001$ for T1-T2 signals compared to different time points.

to the degradation of UMC in TME resulting in the release of Mn^{2+} (Figure 6A and C). These results may be related to the synergistic effect between magnetic targeting and EPR effect. Fluorescence images were acquired by the IVIS Spectrum Imaging System at predetermined time points. The results showed that the tumor fluorescence intensity reached a maximum value 6 h after I.V. (Figure 7A) and remained partially fluorescent after 24 h, indicating that UMC reached the tumor tissue with a long residence time. In vitro fluorescence images of tumors and major organs were obtained 24 h after injection (Figure 7A, right section). It can be seen that UMC mainly stays in the kidney and a small amount accumulates in the liver, suggesting that it is mainly excreted through the kidney. The FL imaging capability of UMC allows us to directly observe its distribution behavior in vivo and provide imaging guidance for cancer therapy.

We also performed PA imaging experiments to confirm the accumulation and degradation of UMC in the tumor area. Figure 7B and C showed that UMC had the strongest signal at 4 h after tail vein injection, mainly because UMC accumulated in the tumor area and did not respond to stimulation in TME. At this time, UMC has not been fully degraded. The signal remained high at 24 h, suggesting that UMC allowed for effective accumulation and retention in the tumor area. Furthermore, as mentioned previously, UMC accumulation can be followed by the release of Mn^{2+} and O_2 depending on the degradation of the tumor environment. This process may be accompanied by improved hypoxic conditions in TME. To validate this process, we monitored oxygenated hemoglobin (HbO_2) production in real-time using the MSOT system. Figure 7B and D showed a gradual increase in the intensity of HbO_2 signal at the tumor site in the

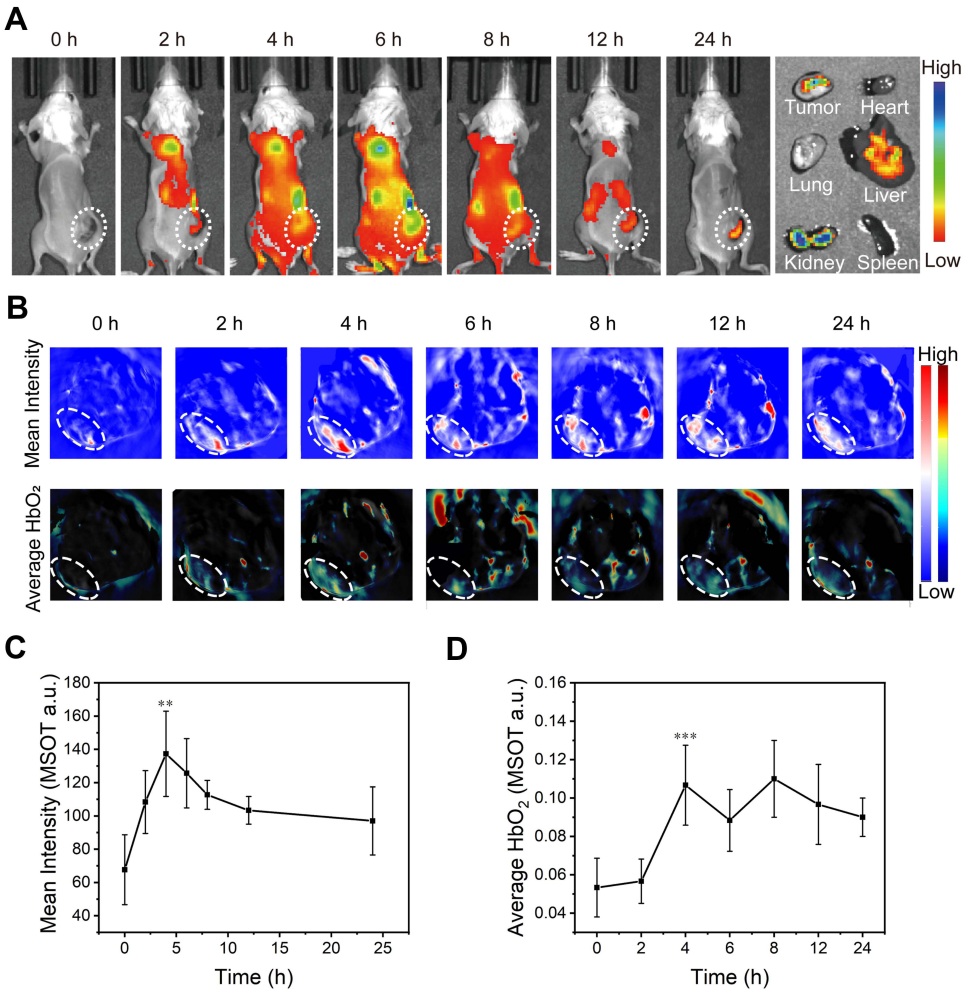

Figure 7 In vivo PA imaging. (**A**) The Fluorescence imaging and (**B**) PA imaging and multispectral optoacoustic tomography imaging of 4T-1 tumor-bearing mice at 0, 2, 4, 6, 8, 12, and 24 h after intravenous tail injection of UMC (USPIO: 20 mg/kg, MnO_2: 20 mg/kg). (**C**) Quantitative analysis of the PAI signal and (**D**) mean oxyhemoglobin value at the corresponding time point in (**A**). $^{**}P < 0.01$ and $^{***}P < 0.001$ for PAI signal and HbO_2 compared to different time points.

UMC group, indicating that oxygen might be released during the degradation of UMC, and the release of oxygen increased the oxygenated hemoglobin content in deoxyhemoglobin.[45]

Antitumor Efficacy of USPIO@MnO_2@Ce6 in vivo

According to the MRI and PAI results, UMC can effectively accumulate at the tumor site through EPR effect and magnetic targeting to release oxygen in the tumor area and enhance the effect of photodynamic therapy. Therefore, we further evaluated the antitumor therapeutic effect of PDT on mouse subcutaneous tumor model by tail vein injection of UMC. The treatment protocol is shown in Figure 8A. When the average tumor volume reaches approximately 70 mm^3, the tumor-bearing mice were randomly divided into six groups: (1) PBS, (2) PBS + laser, (3) Ce6, (4) Ce6 + laser, (5) UMC, and (6) UMC + laser. After injection of different drugs, laser irradiation (660 nm, 20 mW/cm^2, 10 min) was performed, and the drugs were administered once every other day (three times). The body weight and tumor volume of each mouse were recorded every other day for 14 consecutive days. The post-treatment images of each group are shown in Figure S10. Figure 8B and E showed that the treatment effect of the single drug treatment group (Ce6 + laser) was limited compared with the PBS group, PBS + laser group, Ce6 group and UMC group. Although the tumor growth was

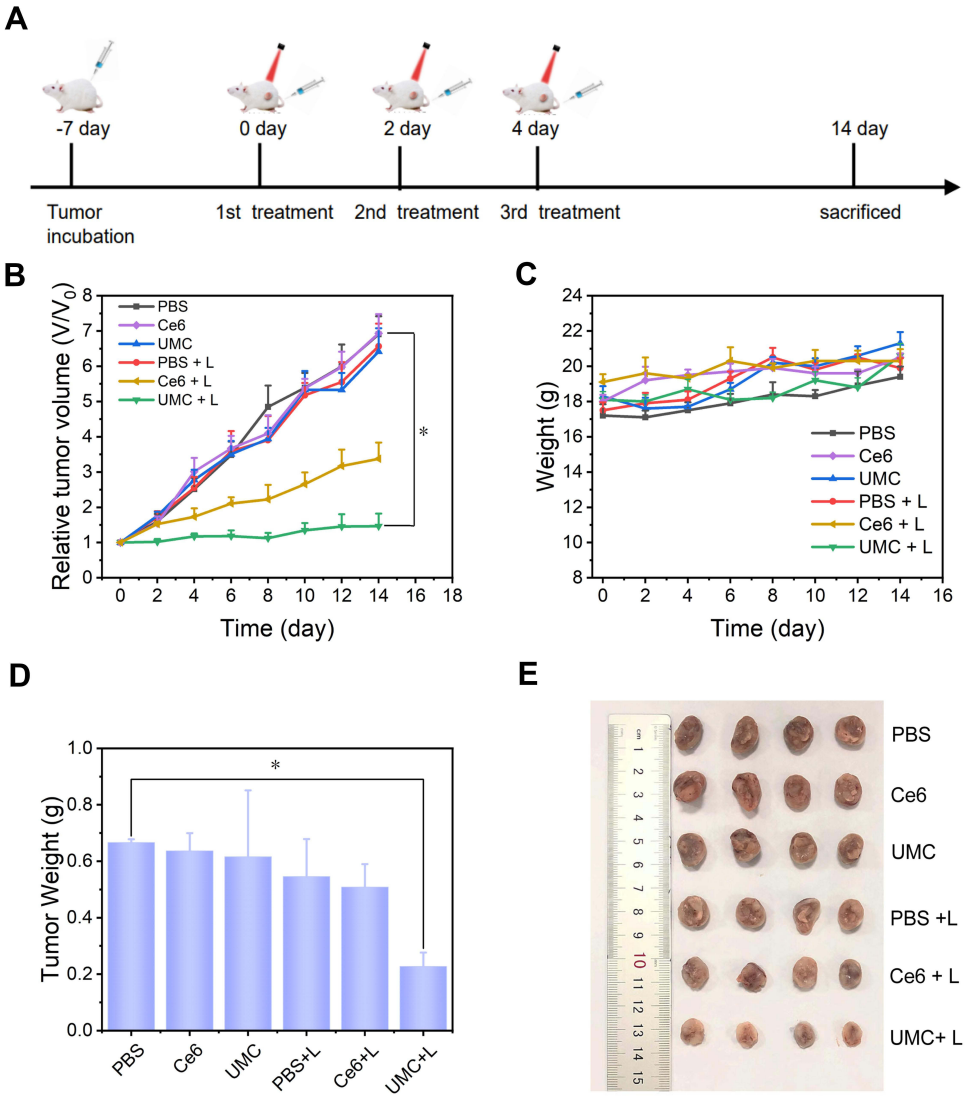

Figure 8 In vivo therapy. (**A**) Schematic diagram of tumor treatment by UMC in vivo. (**B**) Relative tumor volume and (**C**) body weight of mice in different treatment groups within 14 days. (**D**) Tumor weights and (**E**) digital images of tumors in different treatment groups after 14 days of treatment. *Indicates $P < 0.05$ between PBS and UMC + laser group.

slowed down, it could not effectively inhibit tumor growth. This is mainly due to the poor targeting of hydrophobic drugs to tumors and the hypoxic environment of tumors.

The antitumor performance of the UMC + laser group was significantly better than that of the single treatment group. Tumor growth was notably inhibited in the treatment group at the beginning of the treatment. There was no obvious increase in tumor size after treatment, indicating that the combination of MnO_2 and PDT successfully released oxygen, thus improving the efficiency of PDT. This result was further supported by the weight of the tumors removed from the mouse (Figure 8D). The weight of the mice was recorded during the treatment. It was found that there was a slight upward trend in the body weight of mice within 14 days, indicating that UMC had no significant toxicity in vivo (Figure 8C). The anesthetized mice were executed and the hearts, livers, spleens, lungs, kidneys and tumors were taken for H&E staining after the treatment. Notably, no significant histological changes were observed in the major organs of both the control and treated groups, indicating that UMC had good biosafety and biocompatibility (Figure 9).

Discussion

We recently proposed a novel nano-snowflake nanoprobe with high loading efficiency and TME controlled degradability, USPIO@MnO_2@Ce6 (UMC), using T1-T2 MRI and PAI for imaging guidance of tumor treatment. The aim of this study was to confirm the biological applicability of this newly developed probe for multimodality imaging. We evaluated the r1 and r2 relaxation rates and PAI signal changes of UMC using a 7.0 T MRI scanner and MSOT. A study conducted by another research group also found that the relaxation rate of nanoprobes loaded with USPIO increased after the pH/H_2O_2 response.[18] The reason for this phenomenon may be the deterioration of the solution stability after UMC response to TME, resulting in extensive aggregation of USPIO, which exhibits T1 imaging in the dispersed state and T2 imaging in the aggregated state.[44]

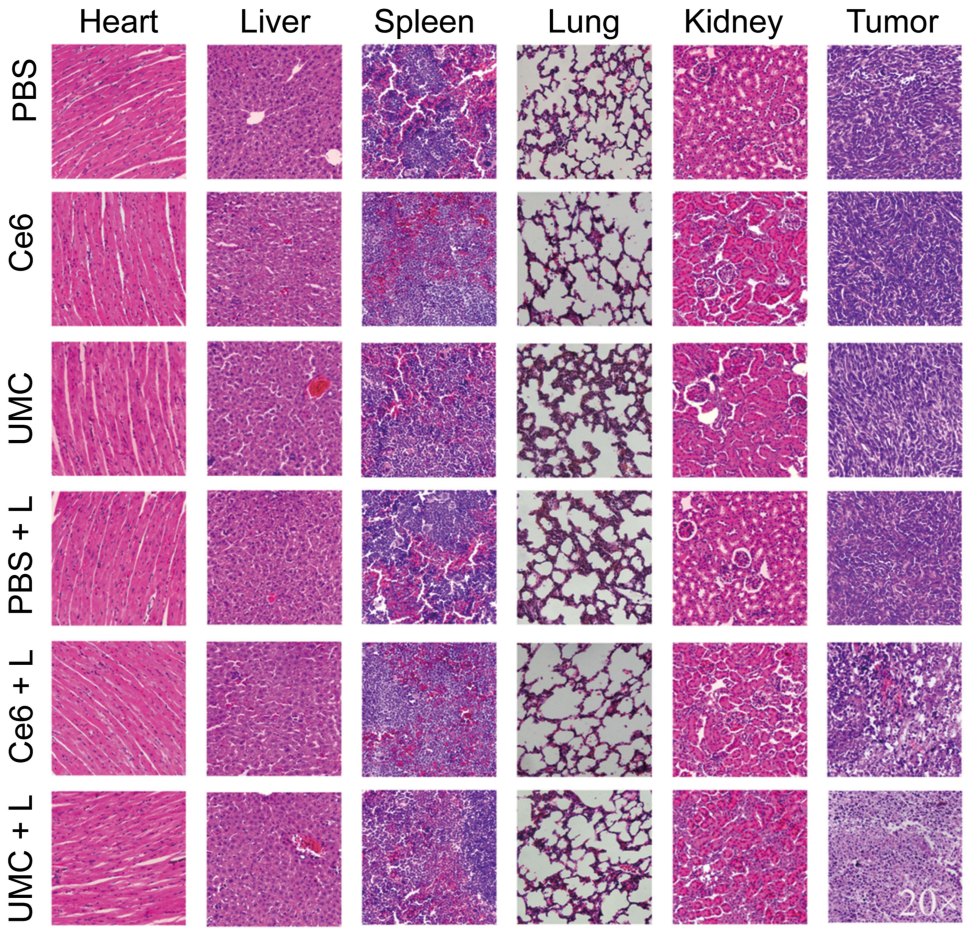

Figure 9 H&E-stained slice images of major organs and tumors from different groups after 14 days (magnification: 200X).

When UMC reacts with H^+ and overexpressed H_2O_2 in TME, the solution stability changes causing the aggregation of USPIO to increase the r2 relaxation rate. Therefore, the enhanced T1-T2 MRI contrast and signal changes in PAI after TME response could theoretically provide accurate imaging guidance for tumor treatment. In order to determine whether UMC can effectively gather in tumors and whether MRI/PAI can effectively visualize in real time after tail vein injection, it is applied to a subcutaneous tumor model in BALB/c mice to explore the effects of multimodality imaging. The MRI results showed that the T1 and T2 signals were the strongest with the most release of Mn^{2+} and USPIO at 6 h. Compared with the MRI results, the PAI results showed that UMC aggregation was the largest at 4 h, and the PAI signal began to weaken at 6 h, indicating that the degradation of UMC and release of Mn^{2+}, which was consistent with the MRI results. This time point was used for subsequent in vivo treatment. Based on the MR/PA imaging results, it was found that the imaging contrast effect was obvious at 6 h when the drug started to be released, and this time point was used for subsequent tumor treatment. In TME, UMC provided a constant source of O_2 for PDT due to the degradation, resulting in elevated ROS levels with the 660 nm laser. Indeed, the UMC + laser group can improve the effectiveness of cancer treatment compared with various other treatments (such as free Ce6). Although the UMC group demonstrated (during in vivo imaging) drug enrichment at the tumor site, this enrichment due to EPR effect and magnetic targeting seemed insufficient to support effective photodynamic therapy. Recently, Professor W.C. Chan[46] also demonstrated a minor effect of EPR on nanoparticles targeting and delivery to the TME. Therefore, finding more suitable targets and avoiding the in vivo circulation process is necessary. The protein crown effect describes a phenomenon in which synthetic nanomaterials are rapidly labeled and encapsulated by serum proteins upon entry into the bloodstream, subject to factors such as immunogenicity. The formation of protein crowns will reshape the metabolic behavior of nanocarriers in vivo, causing non-specific phagocytosis while triggering a series of side effects including autoimmune response, apoptosis or necrosis and inflammation. In recent years, Chen et al[47] identified the protein corona effect also restricted the delivery efficiency of nanomedicine and affected drug release in animals, which might also contribute to the poor therapeutic effect.

There are also certain limitations to this study. First, a subcutaneous tumor-bearing model was selected in this study, and the cell line was derived from mice. This model is not representative of actual clinical practice. Whether UMC can play a role in the clinical diagnosis and treatment of breast cancer needs to be investigated in future studies. Second, PAI only monitored the increased HbO_2 content after UMC reached the tumor region. However, from this result, it seems that the production of O_2 is much lower compared with the cellular level, mainly because the enrichment of UMC reaching the tumor area is not high enough. Therefore, the follow-up study did not assess ROS expression and hypoxia factors in tumor tissue. Although the H_2O_2 content in the TME is high compared to normal cells, this content is still insufficient to support effective O_2 production, which is one of the main reasons limiting the effectiveness of PDT. Therefore, our group will further explore a nanoprobe that can increase the H_2O_2 content in the TME to enhance the therapeutic effect of PDT treatment.

Although UMC has demonstrated some magnetic targeting ability, specific imaging ability and responsive drug release ability, further search for targets that can enhance drug tumor targeting is urgently needed. Interestingly, studies in recent years have revealed a strong affinity between homologous tumor cells, making it easy for cancer cells to accumulate and form solid tumors.[48] This homotypic accumulation is closely related to the recognition and interaction of proteins on the cell membrane.[49,50] Inspired by this concept, tumor cell membranes have recently been used for the design of functional nanostructures for immune escape as well as for the tumor targeting. Usually, these cell membrane-encapsulated nanoparticles have good colloidal stability and biocompatibility and are well targeted to tumors.[51,52] This will also be one of the directions of our future research.

Overall, the results of our study suggested that UMC was a multimodal imaging contrast agent for MRI/PAI, and UMC showed great potential for imaging-guided PDT therapy.

Conclusion

In summary, we prepared a novel snowflake nanoprobe responsive to pH/H_2O_2 in TME. Compared with previously reported manganese dioxide nanostructures, our synthesized honeycomb manganese dioxide nanoparticles have higher drug loading, solution stability, and controlled degradability in TME. In the acidic media, UMC could be decomposed into Mn^{2+} to not only realize drug release but also activate enhanced T1 and T2-weighted MRI contrast. Multifunctional nanoprobes have outstanding oxygen generating capacity, controlled drug release and other properties, resulting in the multimodal imaging and enhanced PDT therapeutic effect. MR and PA imaging were also sensitive to localize the tumor.

In vitro and in vivo antitumor therapy, the nanoprobe allowed oxygen-enhanced PDT guided by T1-T2 MRI and PAI. Compared with free Ce6 group, UMC + laser treatment group showed oxygen-enhanced PDT treatment effect. These results showed that UMC had good potential for clinical applications due to its ability to effectively inhibit tumor growth.

Abbreviations

UMC, USPIO@MnO_2@Ce6; MRI, magnetic resonance imaging; PAI, photoacoustic imaging; USPIO, ultra-small superparamagnetic iron oxide nanoparticles; Ce6, Chlorin e6; TME, tumor microenvironment; ROS, reactive oxygen species; EPR effect, enhanced permeability and retention effect; ROI, regions of interest; MSOT, multispectral optoacoustic tomographic; PDT, photodynamic therapy.

Acknowledgments

The authors thank the National Natural Science Foundation of China (No. 81641074, 11805247); Shandong Provincial Key Research and Development Project (No. 2018YFJH0501); and the Science and Technology Planning Projects of Shandong Provincial Education Department (J17KB082) for the research grants.

Disclosure

The authors report no conflicts of interest in this work.

References

1. Chen H, Qiu Y, Ding D, et al. Gadolinium-encapsulated graphene carbon nanotheranostics for imaging-guided photodynamic therapy. *Adv Mater*. 2018;30(36):e1802748. doi:10.1002/adma.201802748
2. Liu WL, Liu T, Zou MZ, et al. Aggressive man-made red blood cells for hypoxia-resistant photodynamic therapy. *Adv Mater*. 2018;30(35):e1802006. doi:10.1002/adma.201802006
3. Sun S, Chen J, Jiang K, et al. Ce6-modified carbon dots for multimodal-imaging-guided and single-NIR-laser-triggered photothermal/photodynamic synergistic cancer therapy by reduced irradiation power. *ACS Appl Mater Interfaces*. 2019;11(6):5791–5803. doi:10.1021/acsami.8b19042
4. Zhang N, Zhao F, Zou Q, et al. Multitriggered tumor-responsive drug delivery vehicles based on protein and polypeptide coassembly for enhanced photodynamic tumor ablation. *Small*. 2016;12(43):5936–5943. doi:10.1002/smll.201602339
5. Karakashev SV, Reginato MJ. Progress toward overcoming hypoxia-induced resistance to solid tumor therapy. *Cancer Manag Res*. 2015;7:253–264. doi:10.2147/CMAR.S58285
6. Li HJ, Du JZ, Liu J, et al. Smart superstructures with ultrahigh pH-sensitivity for targeting acidic tumor microenvironment: instantaneous size switching and improved tumor penetration. *ACS Nano*. 2016;10(7):6753–6761. doi:10.1021/acsnano.6b02326
7. Minchinton AI, Tannock IF. Drug penetration in solid tumours. *Nat Rev Cancer*. 2006;6(8):583–592. doi:10.1038/nrc1893
8. Thakkar S, Sharma D, Kalia K, et al. Tumor microenvironment targeted nanotherapeutics for cancer therapy and diagnosis: a review. *Acta Biomater*. 2020;101:43–68. doi:10.1016/j.actbio.2019.09.009
9. Laurent S, Forge D, Port M, et al. Magnetic iron oxide nanoparticles: synthesis, stabilization, vectorization, physicochemical characterizations, and biological applications. *Chem Rev*. 2008;108:2064–2110.
10. Wang YX. Superparamagnetic iron oxide based MRI contrast agents: current status of clinical application. *Quant Imaging Med Surg*. 2011;1(1):35–40. doi:10.3978/j.issn.2223-4292.2011.08.03
11. Kellar KE, Fujii DK, Gunther WH, et al. NC100150 injection, a preparation of optimized iron oxide nanoparticles for positive-contrast MR angiography. *J Magn Reson Imaging*. 2000;11(5):488–494. doi:10.1002/(SICI)1522-2586(200005)11:5<488::AID-JMRI4>3.0.CO;2-V
12. Marco MD, Sadun C, Port M, et al. Physicochemical characterization of ultrasmall superparamagnetic iron oxide particles (USPIO) for biomedical application as MRI contrast agents. *Int J Nanomed*. 2007;2:609–622.
13. Cheng W, Yuan P, Zhang Y. Magnetic Resonance Imaging (MRI) contrast agents for tumor diagnosis. *J Healthc Eng*. 2013;4(1):23–45. doi:10.1260/2040-2295.4.1.23
14. Liu Y, Bhattarai P, Dai Z, et al. Photothermal therapy and photoacoustic imaging via nanotheranostics in fighting cancer. *Chem Soc Rev*. 2019;48(7):2053–2108. doi:10.1039/c8cs00618k
15. Zhao J, Chen J, Ma S, et al. Recent developments in multimodality fluorescence imaging probes. *Acta Pharm Sin B*. 2018;8(3):320–338. doi:10.1016/j.apsb.2018.03.010
16. Jennings LE, Long NJ. 'Two is better than one'–probes for dual-modality molecular imaging. *Chem Commun (Camb)*. 2009;2009(24):3511–3524.
17. Burke BP, Cawthorne C, Archibald SJ. Multimodal nanoparticle imaging agents: design and applications. *Philos Trans A Math Phys Eng Sci*. 2017;375:2107.
18. Fan S, Zhang Y, Tan H, et al. Manganese/iron-based nanoprobes for photodynamic/chemotherapy combination therapy of tumor guided by multimodal imaging. *Nanoscale*. 2021;13(10):5383–5399. doi:10.1039/D0NR08831E
19. Hou W, Zhao X, Qian X, et al. pH-Sensitive self-assembling nanoparticles for tumor near-infrared fluorescence imaging and chemo-photodynamic combination therapy. *Nanoscale*. 2016;8(1):104–116. doi:10.1039/C5NR06842H
20. Lee J, Lee YM, Kim J, et al. Doxorubicin/Ce6-loaded nanoparticle coated with polymer via singlet oxygen-sensitive linker for photodynamically assisted chemotherapy. *Nanotheranostics*. 2017;1(2):196–207. doi:10.7150/ntno.18576

21. Lee SR, Kim YJ. Hydrophilic chlorin e6-Poly(amidoamine) dendrimer nanoconjugates for enhanced photodynamic therapy. *Nanomaterials*. 2018;8(6):445–457. doi:10.3390/nano8060445
22. Ryu TK, Baek SW, Kang RH, et al. Photodynamic and photothermal tumor therapy using phase-change material nanoparticles containing chlorin e6 and nanodiamonds. *J Control Release*. 2018;270:237–245. doi:10.1016/j.jconrel.2017.12.008
23. Lu Q, Ericson D, Song Y, et al. MnO2 nanotube-based nanoSearchlight for imaging of multiple microRNAs in live cells. *ACS Appl Mater Interfaces*. 2017;9(28):23325–23332. doi:10.1021/acsami.6b15387
24. Yuan J, Cen Y, Kong XJ, et al. MnO2-Nanosheet-modified upconversion nanosystem for sensitive turn-on fluorescence detection of H2O2 and glucose in blood. *ACS Appl Mater Interfaces*. 2015;7(19):10548–10555. doi:10.1021/acsami.5b02188
25. Fan H, Yan G, Zhao Z, et al. A smart photosensitizer-manganese dioxide nanosystem for enhanced photodynamic therapy by reducing glutathione levels in cancer cells. *Angew Chem Int Ed Engl*. 2016;55(18):5477–5482. doi:10.1002/anie.201510748
26. Yang G, Xu L, Chao Y, et al. Hollow MnO2 as a tumor-microenvironment-responsive biodegradable nano-platform for combination therapy favoring antitumor immune responses. *Nat Commun*. 2017;8(1):902. doi:10.1038/s41467-017-01050-0
27. Zhang M, Cao Y, Wang L, et al. Manganese doped iron oxide theranostic nanoparticles for combined T1 magnetic resonance imaging and photothermal therapy. *ACS Appl Mater Interfaces*. 2015;7(8):4650–4658. doi:10.1021/am5080453
28. Zhao Z, Fan H, Zhou G, et al. Activatable fluorescence/MRI bimodal platform for tumor cell imaging via MnO2 nanosheet-aptamer nanoprobe. *J Am Chem Soc*. 2014;136(32):11220–11223. doi:10.1021/ja5029364
29. Luo M, Lv Y, Luo X, et al. Developing smart nanoparticles responsive to the tumor micro-environment for enhanced synergism of thermo-chemotherapy with PA/MR bimodal imaging. *Front Bioeng Biotechnol*. 2022;10:799610. doi:10.3389/fbioe.2022.799610
30. Abbasi AZ, Prasad P, Cai P, et al. Manganese oxide and docetaxel co-loaded fluorescent polymer nanoparticles for dual modal imaging and chemotherapy of breast cancer. *J Control Release*. 2015;209:186–196. doi:10.1016/j.jconrel.2015.04.020
31. Lin T, Zhao X, Zhao S, et al. O2-generating MnO2 nanoparticles for enhanced photodynamic therapy of bladder cancer by ameliorating hypoxia. *Theranostics*. 2018;8(4):990–1004. doi:10.7150/thno.22465
32. Gao S, Wang G, Qin Z, et al. Oxygen-generating hybrid nanoparticles to enhance fluorescent/photoacoustic/ultrasound imaging guided tumor photodynamic therapy. *Biomaterials*. 2017;112:324–335. doi:10.1016/j.biomaterials.2016.10.030
33. Lin X, Fang Y, Tao Z, et al. Tumor-microenvironment-induced all-in-one nanoplatform for multimodal imaging-guided chemical and photothermal therapy of cancer. *ACS Appl Mater Interfaces*. 2019;11(28):25043–25053. doi:10.1021/acsami.9b07643
34. Wang S, You Q, Wang J, et al. MSOT/CT/MR imaging-guided and hypoxia-maneuvered oxygen self-supply radiotherapy based on one-pot MnO2-mSiO2@Au nanoparticles. *Nanoscale*. 2019;11(13):6270–6284. doi:10.1039/C9NR00918C
35. Liu C, Wang D, Zhan Y, et al. Switchable photoacoustic imaging of glutathione using Mno2 nanotubes for cancer diagnosis. *ACS Appl Mater Interfaces*. 2018;10(51):44231–44239. doi:10.1021/acsami.8b14944
36. Fan W, Bu W, Shen B, et al. Intelligent MnO2 nanosheets anchored with upconversion nanoprobes for concurrent pH-/H2O2-responsive UCL imaging and oxygen-elevated synergetic therapy. *Adv Mater*. 2015;27(28):4155–4161. doi:10.1002/adma.201405141
37. Shang J, Xie B, Li Y, et al. Inflating strategy to form ultrathin hollow MnO2 nanoballoons. *ACS Nano*. 2016;10(6):5916–5921. doi:10.1021/acsnano.6b01229
38. Zhang L, Lian J, Wu L, et al. Synthesis of a thin-layer MnO(2) nanosheet-coated Fe(3)O(4) nanocomposite as a magnetically separable photocatalyst. *Langmuir*. 2014;30(23):7006–7013. doi:10.1021/la500726v
39. Mondal J, Srivastava SK. δ-MnO2 nanoflowers and their reduced graphene oxide nanocomposites for electromagnetic interference shielding. *ACS Appl Nano Mater*. 2020;3(11):11048–11059. doi:10.1021/acsanm.0c02247
40. Carron S, Bloemen M, Vander Elst L, et al. Ultrasmall superparamagnetic iron oxide nanoparticles with europium(III) DO3A as a bimodal imaging probe. *Chemistry*. 2016;22(13):4521–4527. doi:10.1002/chem.201504731
41. Fan H, Zhao Z, Yan G, et al. A smart DNAzyme-MnO(2) nanosystem for efficient gene silencing. *Angew Chem Int Ed Engl*. 2015;54(16):4801–4805. doi:10.1002/anie.201411417
42. Yu Y, Li J, Song B, et al. Polymeric PD-L1 blockade nanoparticles for cancer photothermal-immunotherapy. *Biomaterials*. 2022;280:121312. doi:10.1016/j.biomaterials.2021.121312
43. Szatrowski TP, Nathan CF. Production of large amounts of hydrogen peroxide by human tumor cells. *Cancer Res*. 1991;51(3):794–798.
44. Chen A, Lu H, Cao R, et al. A novel MMP-responsive nanoplatform with transformable magnetic resonance property for quantitative tumor bioimaging and synergetic chemo-photothermal therapy. *Nano Today*. 2022;45:23.
45. Yang C, Mi X, Su H, et al. GE11-PDA-Pt@USPIOs nano-formulation for relief of tumor hypoxia and MRI/PAI-guided tumor radio-chemotherapy. *Biomater Sci*. 2019;7(5):2076–2090. doi:10.1039/C8BM01492B
46. Sindhwani S, Syed AM, Ngai J, et al. The entry of nanoparticles into solid tumours. *Nat Mater*. 2020;19(5):566–575. doi:10.1038/s41563-019-0566-2
47. Cai R, Ren J, Guo M, et al. Dynamic intracellular exchange of nanomaterials' protein Corona perturbs proteostasis and remodels cell metabolism. *Proc Natl Acad Sci U S A*. 2022;119(23):e2200363119. doi:10.1073/pnas.2200363119
48. Zhu JY, Zheng DW, Zhang MK, et al. Preferential cancer cell self-recognition and tumor self-targeting by coating nanoparticles with homotypic cancer cell membranes. *Nano Lett*. 2016;16(9):5895–5901. doi:10.1021/acs.nanolett.6b02786
49. Chen HY, Deng J, Wang Y, et al. Hybrid cell membrane-coated nanoparticles: a multifunctional biomimetic platform for cancer diagnosis and therapy. *Acta Biomater*. 2020;112:1–13. doi:10.1016/j.actbio.2020.05.028
50. Yang R, Xu J, Xu L, et al. Cancer cell membrane-coated adjuvant nanoparticles with mannose modification for effective anticancer vaccination. *ACS Nano*. 2018;12(6):5121–5129. doi:10.1021/acsnano.7b09041
51. Zhang Y, Cai K, Li C, et al. Macrophage-membrane-coated nanoparticles for tumor-targeted chemotherapy. *Nano Lett*. 2018;18(3):1908–1915. doi:10.1021/acs.nanolett.7b05263
52. Wang C, Wang Y, Zhang L, et al. Pretreated macrophage-membrane-coated gold nanocages for precise drug delivery for treatment of bacterial infections. *Adv Mater*. 2018;30(46):e1804023. doi:10.1002/adma.201804023